scientific reports

Check for updates

OPEN

# SCAPS simulation of novel inorganic $ZrS_2$/CuO heterojunction solar cells

Mahmoud Abdelfatah[1]✉, Adel M. El Sayed[2], Walid Ismail[1], Stephan Ulrich[3], Volker Sittinger[3] & Abdelhamid El-Shaer[1]✉

**$ZrS_2$ is transition metal dichalcogenides (TMDCs) which is believed one of the most talented applicants to fabricate photovoltaics. Therefore, we present here for the first-time numerical simulation of novel inorganic $ZrS_2$/CuO heterojunction solar cells employing SCAPS-1D. The influence of the thickness, carrier concentration, and bandgap for both the window and absorber layers on the solar cell fundamental parameters was explored intensely. Our results reveal that the solar cell devices performance is mainly affected by many parameters such as the depletion width ($W_d$), built-in voltage ($V_{bi}$), collection length of charge carrier, the minority carrier lifetime, photogenerated current, and recombination rate. The η of 23.8% was achieved as the highest value for our simulated devices with the $V_{oc}$ value of 0.96 V, the $J_{sc}$ value of 34.2 mA/cm$^2$, and the FF value of 72.2%. Such efficiency was obtained when the CuO band gap, thickness, and carrier concentration were 1.35 eV, 5.5 µm, and above $10^{18}$ cm$^{-3}$, respectively, and for the $ZrS_2$ were 1.4 eV, 1 µm, and less than $10^{20}$ cm$^{-3}$, respectively. Our simulated results indicate that the inorganic $ZrS_2$/CuO heterojunction solar cells are promising to fabricate low-cost, large-scale, and high-efficiency photovoltaic devices.**

Currently, the demand for energy increase year by year, which is important for technological and industrial development worldwide although limited fossil fuels[1]. Solar cells are considered one of the highly significant renewable energy sources since they are environmental ecofriendly technology to reduce global $CO_2$ emissions[1].

Recently, transition metal dichalcogenides (TMDCs) have received high attention to become potential candidates instead of traditional materials for various applications especially solar cells[2,3] as well as batteries[4], photodetector[5,6], biomedical[7], and catalysis[8]. In these materials, the d- d transition positioned at a metal site producing large band-edge excitation and therefore unique electronic properties leading for such various applications.

Zirconium disulfide ($ZrS_2$), belongs to group IV of TMDCs, is n-type semiconductor which reveals a low mismatch lattice with other absorber materials because of Van-der-Waals force (VdW) force[2,9]. $ZrS_2$ is considered as a powerful applicant to fabricate optoelectronics particularly photovoltaics since it has high absorption coefficient and bandgap energy that could be easily engineered to be in the range of 1.2–2.2 eV[2,3,10]. Moreover, $ZrS_2$ has several unique electronic and optical properties owing to quasi 2D characteristic[2]. Based on these properties, $ZrS_2$ could be utilized in many fields besides solar cells[2,3] such as field-effect transistors (FETs)[11], lithium-ion batteries[12], water-splitting[13], photocatalysis[14], lubricant additives[15], and photodetectors[16].

Tunable of bandgap energy as well as electronic and optical properties for $ZrS_2$ thin film could be achieved employing several growth techniques like chemical vapor deposition (CVD)[11], chemical vapor transport (CVT)[17], atomic layer deposition (ALD)[13,18], sputtering[19], and liquid exfoliation method[9].

On the other hand, CuO is a semiconductor that has bandgap in the range of 1.2–1.5 eV, good thermal and electronic features and generally used in superconductors, supercapacitors, and solar energy purposes[20]. In addition, $Cu_2O$ is a non-toxic material and has a narrow direct optical band gap in the range of 1.9–2.3 eV and therefore employed on optoelectronic devices[21]. The combination of *n*-$ZrS_2$ thin films with other *p*-type semiconductors with appropriate energy level alignment such as CuO and $Cu_2O$ as well as buffer layers like graphene oxide could be future key to have solar cells with higher efficiency[22–25].

The predication of the optimum parameters for the materials is considered one the most promising keys to fabricate high performance solar cells. The simulation is a valuable approach to examine the influence of changes

[1]Physics Department, Faculty of Science, KafrelSheikh University, KafrelSheikh 33516, Egypt. [2]Physics Department, Faculty of Science, Fayoum University, Fayoum 63514, Egypt. [3]Fraunhofer Institute for Surface Engineering and Thin Films IST, Bienroder Weg 54E, 38108 Braunschweig, Germany. ✉email: mahmoud.abdelfatah@sci.kfs.edu.eg; elshaer@sci.kfs.edu.eg

in material properties on the solar cell basic parameters and study the complex heterogeneous absorber/buffer interfaces. Therefore, many papers were published to predicate the solar cells efficiencies employing Solar Cell Capacitance Simulator Structures (SCAPS-1D) software, which is a one-dimensional (1D) windows-oriented program and has the largest number of simulation parameters[26–29].

Consequently, we present here for the first-time SCAPS numerical simulation of novel inorganic $ZrS_2$/CuO heterojunction solar cell devices. Typically, the effect of the thickness, carrier concentration, and bandgap for both the window and absorber layers on the solar cell fundamental parameters will be investigated deeply. Our simulated results will be step forwards to know the optimum parameters to experimental produce high efficiency photovoltaic devices.

## Materials and methods

**Inorganic solar cell structure.** Figure 1 represents a schematic diagram of the heterojunction device structure that was employed in the simulation. Typically, n-$ZrS_2$ thin film was used as the window layer, while p-CuO thin film was employed as the absorber layer to shape our inorganic p–n heterojunction solar cells. Transparent conductive oxide (TCO) and Gold (Au) were utilized as the front and the back metal contacts for the device.

**Numerical simulation and parameters of materials.** In our current research, SCAPS-1D software[30–32], as a powerful and valuable numerical simulation tool to recognize and clarify the physical phenomena arising in photovoltaic devices, was utilized to simulate and evaluate our inorganic solar cells. The light intensity of AM 1.5 light spectrum (100 mW/cm$^2$), as standard testing conditions (STC), were employed in all SCAPS-1D simulation calculations. Here, impact of bandgap, thickness, and carrier concentration of both the absorber and window layers on the solar cell fundamental parameters were analyzed intensely where different values for input variable were used to obtain optimum values to have higher performance of solar cell devices.

The following Poisson and continuity equation for holes and electrons are used in SCAPS-1D numerical simulation calculations[33,34]

$$\frac{d^2}{dx^2}\Psi(x) = \frac{e}{\varepsilon_0 \varepsilon_r}\left(p(x) - \mathrm{n(x)} + N_D - N_A + \rho_{defect}(\mathrm{p(x)}, \mathrm{n(x)})\right) \quad (1)$$

$$\frac{dJ_n}{dx} = \mathrm{G} - \mathrm{R} \text{ and } \frac{dJ_p}{dx} = \mathrm{G} - \mathrm{R} \quad (2)$$

where $\boldsymbol{\Psi}$, $\mathbf{e}$, $\boldsymbol{\varepsilon_0}$, $\boldsymbol{\varepsilon_r}$, $\mathbf{p}$, $\mathbf{n}$, $\mathbf{N_D}$, $\mathbf{N_A}$, $\boldsymbol{\rho_{defect}}$, $\mathbf{J_n}$, $\mathbf{J_p}$, $\mathbf{R}$, and $\mathbf{G}$ are electrostatic potential, charge of electron, vacuum permittivity, relative permittivity, hole density, electron density, donor impurities, acceptor impurities, distribution of defects, current densities of electron, current densities of hole, recombination rate, and generation rate, respectively. The parameters of $ZrS_2$ and CuO thin films applied to execute our numerical simulations are scheduled in Table 1 according to Refs.[2,25,35,36].

## Results and discussion

**Impact of CuO thickness, bandgap, and carrier concentration on basic parameters of solar cells.** In this section, we firstly study effect of the absorber layer thickness, band gap, and carrier concentrations on the photovoltaic fundamental parameters (open circuit voltage ($V_{oc}$), short circuit current density ($J_{sc}$), fill factor (FF), and cell efficiency (η)) where the window layer thickness, band gap, and carrier concentration are fixed at 0.2 µm, 1.7 eV, $10^{19}$ cm$^{-3}$, respectively.

Figure 2 demonstrates the gained contour plot of the modelled solar cell basic parameters including $V_{oc}$, $J_{sc}$, FF, and η as the CuO layer thickness and the band gap vary from 1 to 6 µm (the x-axis) and from 1 to 1.5 eV (the y-axis), respectively.

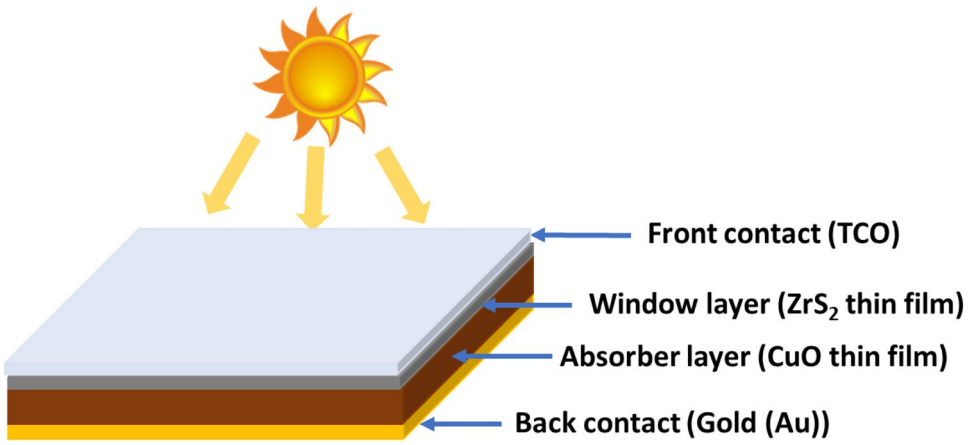


**Figure 1.** Schematic structure of inorganic $ZrS_2$/CuO heterojunction solar cell.

| Material parameter | n-$ZrS_2$ | p-CuO |
|---|---|---|
| Dielectric permittivity | 16.4 | 18.1 |
| Bandgap (eV) | 1.7 | 1.2 |
| Electron affinity (eV) | 4.7 | 4.07 |
| Effective density of states of valence band maximum ($cm^{-3}$) | $1.8\times10^{19}$ | $5.5\times10^{20}$ |
| Effective density of states of conduction band minimum ($cm^{-3}$) | $2.2\times10^{19}$ | $3\times10^{19}$ |
| Acceptor concentration ($cm^{-3}$) | 0 | $10^{16}$ |
| Donor concentration($cm^{-3}$) | $10^{19}$ | 0 |
| Mobility of Hole ($cm^2/(V\cdot s)$) | 30 | 20 |
| Mobility of Electron ($cm^2/(V\cdot s)$) | 300 | 200 |
| Electron thermal velocity (cm/s) | $10^7$ | $10^7$ |
| Hole thermal velocity (cm/s) | $10^7$ | $4.6\times10^6$ |

**Table 1.** Material parameters employed in our simulations[2,25,35,36].

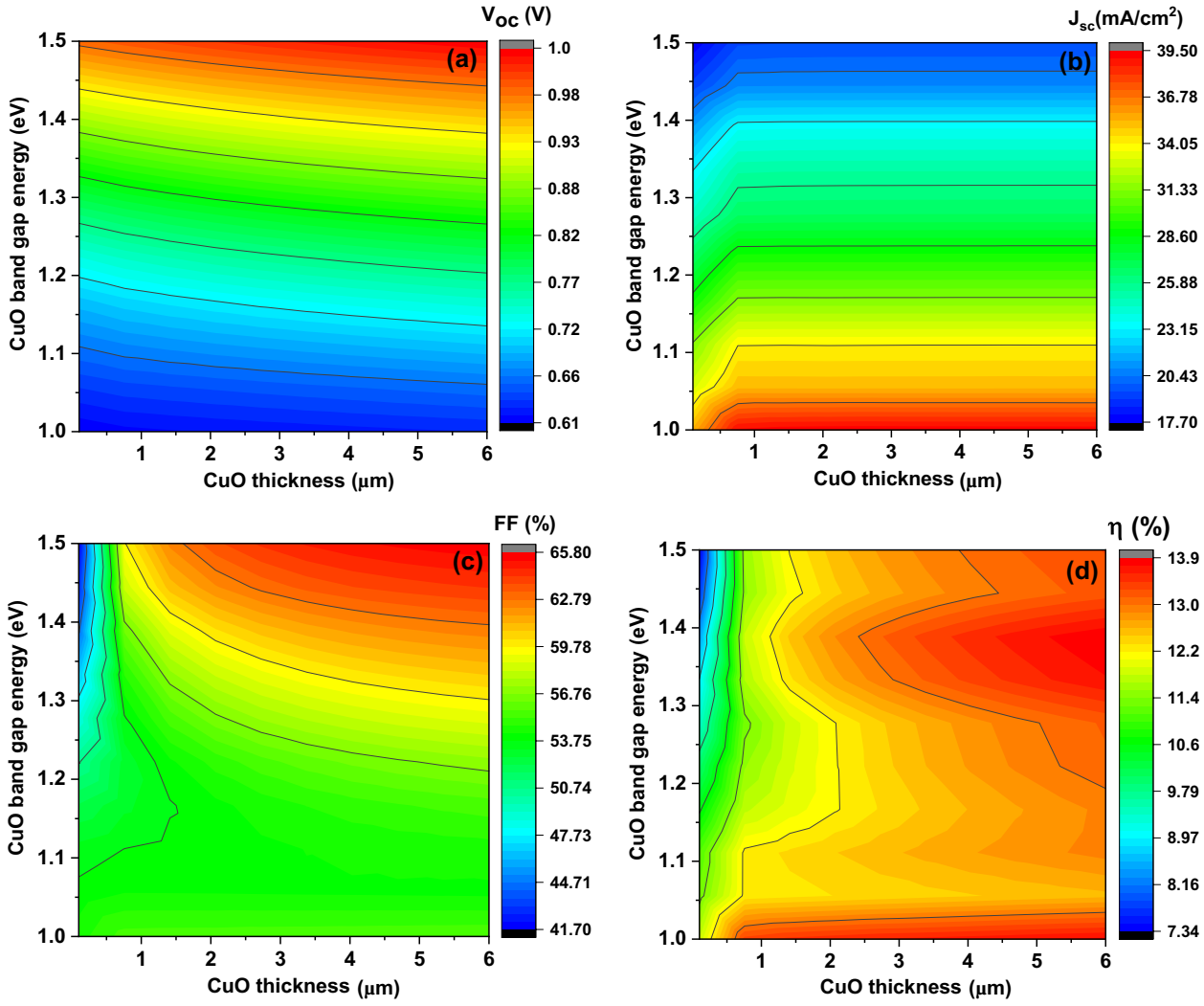


**Figure 2.** The simulated solar cells basic parameters including $V_{oc}$ (**a**), $J_{sc}$ (**b**), FF (**c**), and η (**d**) as function on the absorber layer thickness (x-axis) and the band gap (y-axis) at acceptor concentration $10^{16}$ $cm^{-3}$.

It is clear from Fig. 2a that $\mathbf{V_{oc}}$ increases from about 0.61 V at $\mathbf{E_g}$ of 1 eV to about 1 V at $\mathbf{E_g}$ of 1.5 eV while the variation of the $\mathbf{V_{oc}}$ with CuO thickness rise from 1 to 6 μm for any Eg did not excess more than 0.1 V. The $\mathbf{J_{sc}}$ value is observed to decline from about 39.5 to 17.7 mA/$cm^2$ with the increase of the $\mathbf{E_g}$ from 1 to 1.5 eV as presented in Fig. 2b. The $\mathbf{J_{sc}}$ values remain almost constant for each CuO thickness which varied from 1 to 6 μm.

Figure 2c indicates that the FF values are varying in different ways where firstly FF decreases from about 55% to about 41.7% with increasing of the $\mathbf{E_g}$ from 1 to 1.5 eV and this at the same time of increasing CuO thickness from about 0.1–1.5 µm (thinner CuO thin films). Secondly, FF grows from about 55% to about 65.8% with raising of the $\mathbf{E_g}$ from 1 to 1.5 eV and this take place with CuO thickness increasing from about 1.5–6 µm (thicker CuO thin films) with reducing on the value of FF of about 3%.

Figure 2d reveals that the η values have different zones where η of about 13.3% is detected at the $\mathbf{E_g}$ of about 1 eV with thickness increasing from about 0.5 to 6 µm. η with average value of about 12.5% is achieved for almost variation of the $\mathbf{E_g}$ from 1 to 1.5 eV expect zone located at the $\mathbf{E_g}$ from 1.3 to 1.45 eV and the thickness from 3 to 6 µm where higher performance of about 13.86% is obtained.

These results could be clarified as the band gap increasing, the local collection efficiency of light absorption increase inside the interface of the p-CuO thin film and n-$ZrS_2$ thin film and enhances the carrier generation rate and therefore increasing the value of the $\mathbf{V_{oc}}$ dramatically according to the following equation[37]:

$$V_{oc} = \frac{k_B T}{q} \ln\left(1 + \frac{I_{ph}}{I_0}\right) \tag{3}$$

Also, this explained whereas based on the $ZrS_2$ and CuO bandgap values, band alignment of a cliff-like is supposed leading to improve the charge separation process[2]. When the bandgap energy raises, the valence band **Ev** shifts downward while the conduction band **Ec** shifts upper producing decreasing on the conduction band offset (**ΔEc**) value[2]. The lowered **ΔEc** helps the charge separation process with more approachable promotion electrons to the absorber layer and transport through the interface into the window layer and therefore enhancement of the $\mathbf{V_{oc}}$[2]. While band gap increasing producing high hole concentrations close to the interface junction. Therefore, increasing the probability of the recombination rate happens through surface and facing interface recombination. Consequently, this explained reducing of the $\mathbf{J_{sc}}$ with increasing band gap[2,38]. Moreover, the wavefunction intersecting between vibrational excited states of the lower and the higher lying electronic states produce capture centers for charge carriers[38].

The behavior of the **FF** is always effected by many factors especially the series and shunt resistance as well as partially the $\mathbf{V_{oc}}$ values as presented in the following equation[39]:

$$\mathrm{FF} = \frac{\upsilon_{oc} - \ln(\upsilon_{oc} + 0.72)}{\upsilon_{oc} + 1}, \tag{4}$$

where $\boldsymbol{\upsilon_{oc}} = \mathbf{qV_{oc}/AkT}$.

The η behavior could be illustrated by the behavior and the values of the $\mathbf{V_{oc}}$, the $\mathbf{J_{sc}}$, and the **FF** where the **η** given by the following equation[40]:

$$\eta = \frac{FFV_{oc}J_{sc}}{P_{in}}. \tag{5}$$

From above results we concluded that to have higher efficiencies solar cells, the CuO band gap and thickness should be in the range of 1.35 eV and from 3 to 6 µm, respectively. Therefore, JV curves with basic parameters of solar cells as function of CuO thickness from 3 to 6 µm at constant band gap of 1.35 eV are simulated as described in Fig. 3. It is clear from such figure that the $\mathbf{V_{oc}}$ has value from 0.88 to 0.90 V, the $\mathbf{J_{sc}}$ has constant value of 25.1 mA/cm$^2$, the **FF** has value from 59.9 to 61.3% and the **η** has value from 13.2 to 13.86 with increasing thickness from 3 to 6 µm, respectively where the **η** value follows mainly the $\mathbf{V_{oc}}$, and the **FF** values.

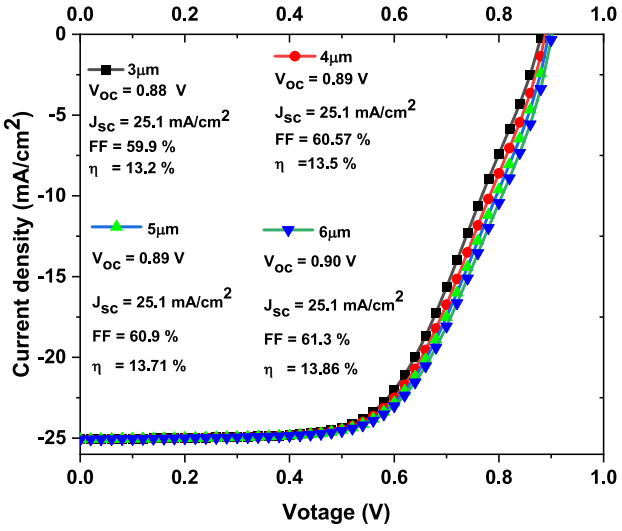


**Figure 3.** The simulated JV curves with basic parameters of solar cells as function on CuO thickness from 3 to 6 µm.

Figure 4 displays the achieved contour plot of the obtained photovoltaic basic parameters consist of $V_{oc}$, $J_{sc}$, FF, and η as function on the CuO thin film thickness and the acceptor concentration differ from 1 to 6 μm (the x-axis) and from $1 \times 10^{14}$ to $1 \times 10^{21}$ $cm^{-3}$ (the y-axis), respectively.

It is apparent from Fig. 4a that the $\mathbf{V_{oc}}$ improves from about 0.72 V to 1 eV as acceptor concentration enhances from $10^{14}$ to $10^{21}$ $cm^{-3}$ with small variation in the $\mathbf{V_{oc}}$ values with rising of CuO thickness. From Fig. 4b, the value of $\mathbf{J_{sc}}$ increases from about 29.5–31.4 $mA/cm^2$ with increasing of acceptor concentration from $10^{17}$ to $10^{21}$ $cm^{-3}$ and the value stays constant at about 29.5 $mA/cm^2$ for carrier concentration less than $10^{17}$ and this at CuO thickness above 1.5 μm. For CuO thickness less than 1.5 μm, the $\mathbf{J_{sc}}$ continues of about 28.3 $mA/cm^2$ for carrier concentration less than $10^{18}$ $cm^{-3}$, while the $\mathbf{J_{sc}}$ value change for carrier concentration above $10^{18}$ $cm^{-3}$ from 24 to 29.5 $mA/cm^2$ with CuO thickness increasing.

Figure 4c implies that the FF values remain mainly constant at value of about 56% for all carrier concentration and thickness expect for carrier concentration from $10^{14}$ to $10^{17}$ $cm^{-3}$, the FF increase from about 50–55% in thickness range from 1 to 3 5 μm. The FF higher value of about 61% is obtained for carrier concentration of $10^{21}$ $cm^{-3}$ and for thickness less than 1 μm.

Figure 4d shows that the η values have the same shape as the $\mathbf{V_{oc}}$ where η increase from about 9.8% to about 12.5% as the carrier concentration increase from $10^{14}$ to $10^{17}$ $cm^{-3}$ and this with thickness growing. The η value of about 12.5% increase to about 18.9% with rising of the carrier concentration from $10^{17}$ to $10^{21}$ $cm^{-3}$.

Such results could be explained as the carrier concentration increasing, the electron diffusion increases from the p-CuO thin film to n-$ZrS_2$ thin film and enhances the value of the device built-in voltage ($\mathbf{V_{bi}}$) which formed mainly by the depletion width ($\mathbf{W_d}$) and therefore the $\mathbf{V_{oc}}$ increases dramatically[37,38]. Moreover, the photogenerated current (electron hole pairs) ($\mathbf{I_{ph}}$) increase and therefore the recombination rate and the reverse saturation current ($\mathbf{I_o}$) will be reduced and therefore enhancement of the $\mathbf{V_{oc}}$ values[41] as presented in Eq. (3) which clear the relation between the $\mathbf{V_{oc}}$, $\mathbf{I_{ph}}$, and $\mathbf{I_o}$ –[42]:

On other hand, the $\mathbf{J_{sc}}$ values improves with increasing of carrier concentration because also enhancement of the photogenerated charge carriers and decreasing of both the leakage current and the recombination current especially for CuO thickness higher than 1.5 μm.

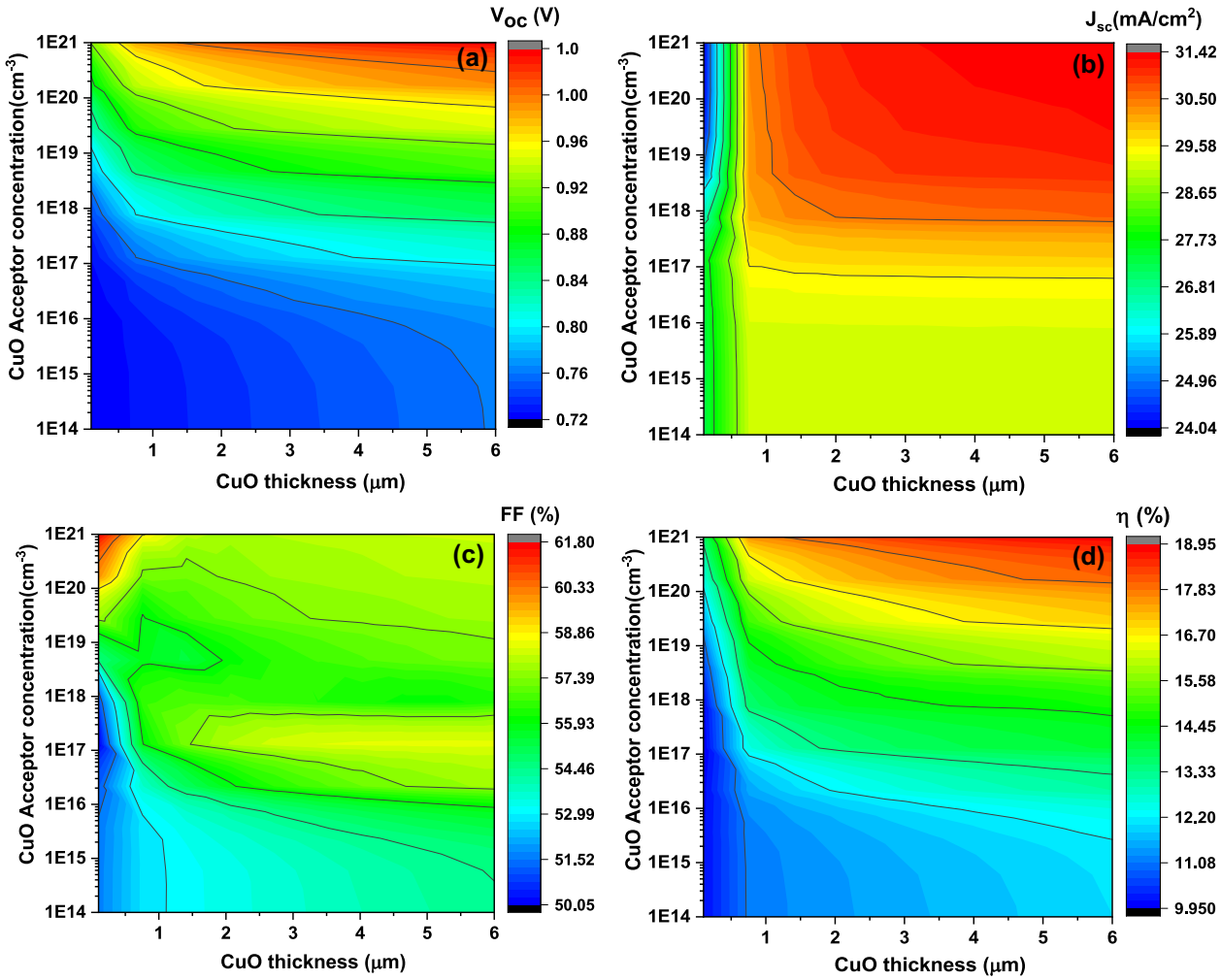


**Figure 4.** The simulated solar cells basic parameters including $V_{oc}$ (**a**), $J_{sc}$ (**b**), FF (**c**), and η (**d**) as function on the absorber layer thickness (x-axis) and the carrier concentration (y-axis) at $E_g = 1.35$ eV.

For the absorber thickness less than 1.5 µm and carrier concentration above $10^{18}$ $cm^{-3}$, the $\mathbf{J_{sc}}$ raise with CuO thickness growing could be ascribed to the CuO charge collection length and hence the collection of electron hole pairs in the junction will be improved[43]. This indicates that the charge carriers will be split up and stored clearly with thickness increasing. For higher carrier concentration than $10^{18}$ $cm^{-3}$ and CuO thickness higher than 1.5 µm, the charge collection length reached the maximum and the carrier collection probability increasing and the recombination rate and leakage current reducing which producing higher values for the $\mathbf{J_{sc}}$[2].

The behavior of the η could be described by the whole behavior of the $\mathbf{V_{oc}}$, the $\mathbf{J_{sc}}$, and the **FF** where the η is a factor of these parameters as shown before in Eq. (5)[40]:

In this case, the shape of the η follows mainly the $\mathbf{J_{sc}}$ shape since the acceptor concentration influence mainly the photogenerated current. Therefore, the external quantum efficiency (EQE) as function on CuO thickness, band gap, and the carrier concentration is recorded as presented in Fig. 5. It is noticeable that EQE have the same shape with all CuO thickness with value of 40% at 200 nm and 100% at 800 nm. With increasing of the band gap from 1 to 1.5 eV, the area under curve for higher EQE part moved downward from 1200 to 800 nm. By increasing the carrier concentration from $10^{14}$ to $10^{21}$ $cm^{-3}$, EQE value improve from around 40–52% for wavelength from 200 to 700 nm, while EQE value reduce from 100 to 90% for higher wavelength from 700 to 1050 nm. Moreover, there is intrinsic absorption edge in the short-wavelength region of the spectrum[41,42] where it positions change with the variation of the carrier concentration as presented in Fig. 5d and this could be attributed to the reflection from the Au back contact[41,42]. The results indicate the photogenerated current increasing with high energy photon while decreasing for lower one and this suppose the different generation and recombination rate of charge carriers that controlled the $\mathbf{J_{sc}}$. The results confirmed and supported that the η will affect mainly by the $\mathbf{J_{sc}}$. We can conclude from the above simulations that the CuO band gap, thickness, and carrier concentration should be in the range of 1.35 eV, 5.5 µm, and above $10^{18}$ $cm^{-3}$, respectively to achieve higher efficiencies for $ZrS_2$/CuO heterojunction solar cell devices.

**Impact of $ZrS_2$ thickness, bandgap, and carrier concentration on basic parameters of solar cells.** Secondly, the influence of the $ZrS_2$ thin film, as window layer, thickness, band gap, and carrier concen-

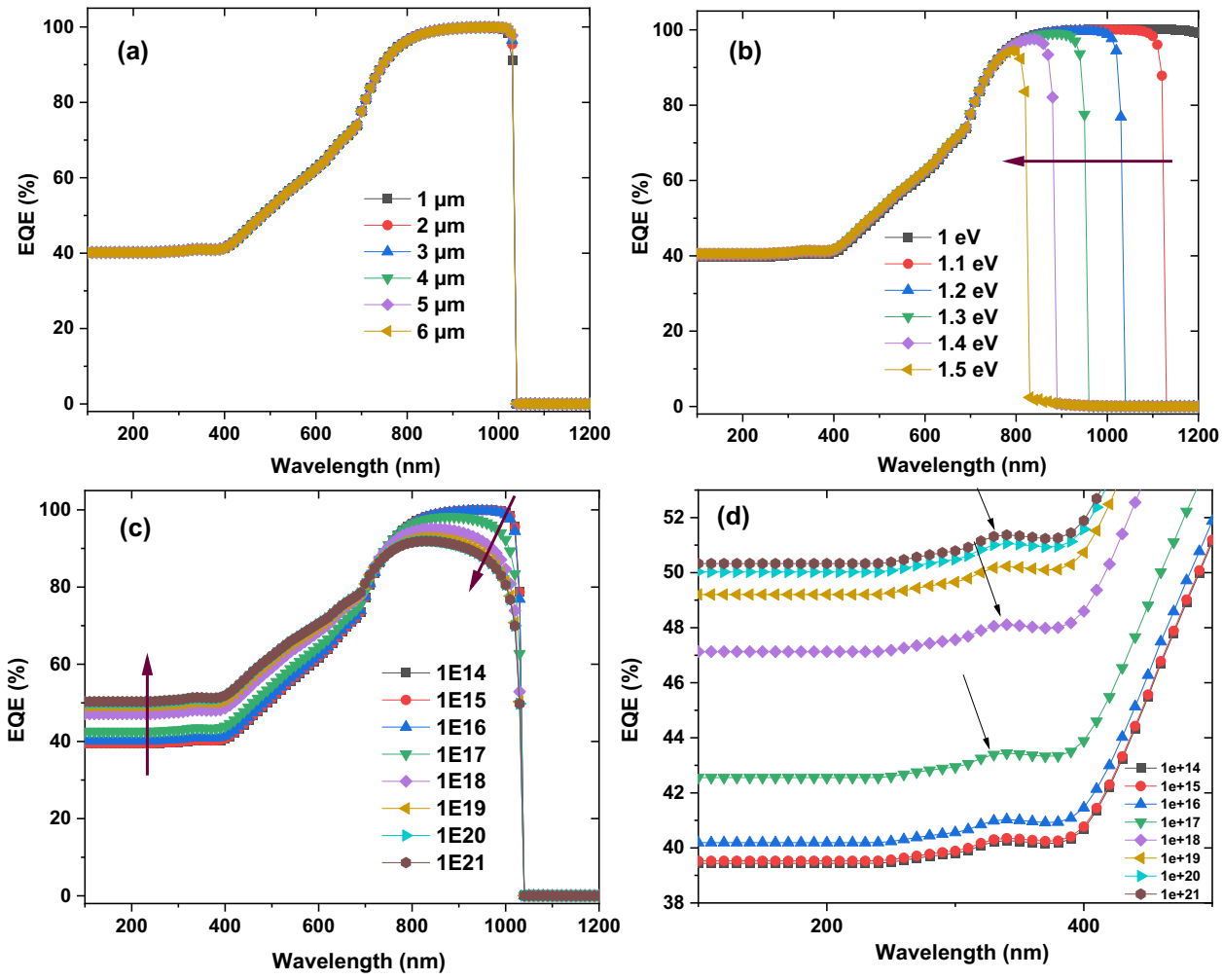


**Figure 5.** The simulated external quantum efficiency as function on CuO thickness (**a**), band gap (**b**), and the carrier concentration (**c,d**) respectively.

trations on the basic parameters of photovoltaic devices will be explored deeply while the CuO layer thickness, band gap, and carrier concentrations are fixed at 5.5 μm, 1.35 eV, $10^{18}$ $cm^{-3}$, respectively.

Figure 6 proves the achieved contour plot of the simulated basic parameters of solar cell as a function on the $ZrS_2$ thin film thickness and the band gap vary from 0.1 to 1 μm (the x-axis) and from 1.3 to 1.8 eV (the y-axis), respectively.

The $\mathbf{V_{oc}}$ has different values with different zones as shown in Fig. 6a. It decreases mainly from about 0.96 V to about 0.87 V with band gap increasing from 1.3 to 1.8 eV. For lower band gap from 1.3 eV to about 1.45 eV, the $\mathbf{V_{oc}}$ value improving for each individual $\mathbf{E_g}$ value with rising $ZrS_2$ thickness. While for intermediate ones from 1.45 eV to about 1.6 eV, the $\mathbf{V_{oc}}$ values remains nearly constant with increasing $ZrS_2$ thickness. For higher band gap than 1.6 eV, the $\mathbf{V_{oc}}$ reducing with increasing $ZrS_2$ thickness.

Figure 6b appears that the $\mathbf{J_{sc}}$ value remains constant at average of about 33.5 $mA/cm^2$ for the $\mathbf{E_g}$ value below 1.55 eV even with increasing $ZrS_2$ thickness. For the $\mathbf{E_g}$ from 1.55 to 1.65 eV, the $\mathbf{J_{sc}}$ value also remains nearly constant with thickness rising with rang from 18 to 25 $mA/cm^2$ for each the $\mathbf{E_g}$ value. On another hand, for higher $\mathbf{E_g}$ values, the $\mathbf{J_{sc}}$ reduces from about 28 $mA/cm^2$ to about 10 $mA/cm^2$ with thickness increasing from 0.1 to 1 μm.

Figure 6c suggests that the FF has different values with the $\mathbf{E_g}$ values. For the $\mathbf{E_g}$ below 1.55 eV, FF increasing with $ZrS_2$ thickness increasing for each individual value of the $\mathbf{E_g}$. For example, at 1.4 eV, FF value increase from about 64% to about 71% with thickness increasing from 0.1 to 1 μm. For intermediate $\mathbf{E_g}$ from 1.55 to 1.65 eV, FF remains constant with thickness growing. For higher $\mathbf{E_g}$ than 1.65 eV, FF values enhance with thickness increasing but with smaller values than lower band gaps. Overall, the FF value increases mainly with $ZrS_2$ thickness increasing.

Figure 6d recognizes that the η has different values where it decreases with thickness increasing for the $\mathbf{E_g}$ below 1.5 eV. For example, at 1.4 eV, the η increases from about 20% to about 23.6% with thickness growth from 0.1 to 1 μm. While for intermediate $\mathbf{E_g}$ values between 1.55 and 1.65 eV, the η values remains nearly constant with thickness increasing. On another hand, for higher $\mathbf{E_g}$, the η reduces with thickness rising for each individual $\mathbf{E_g}$ value. Generally, the η has the same shape as the the $\mathbf{V_{oc}}$ values.

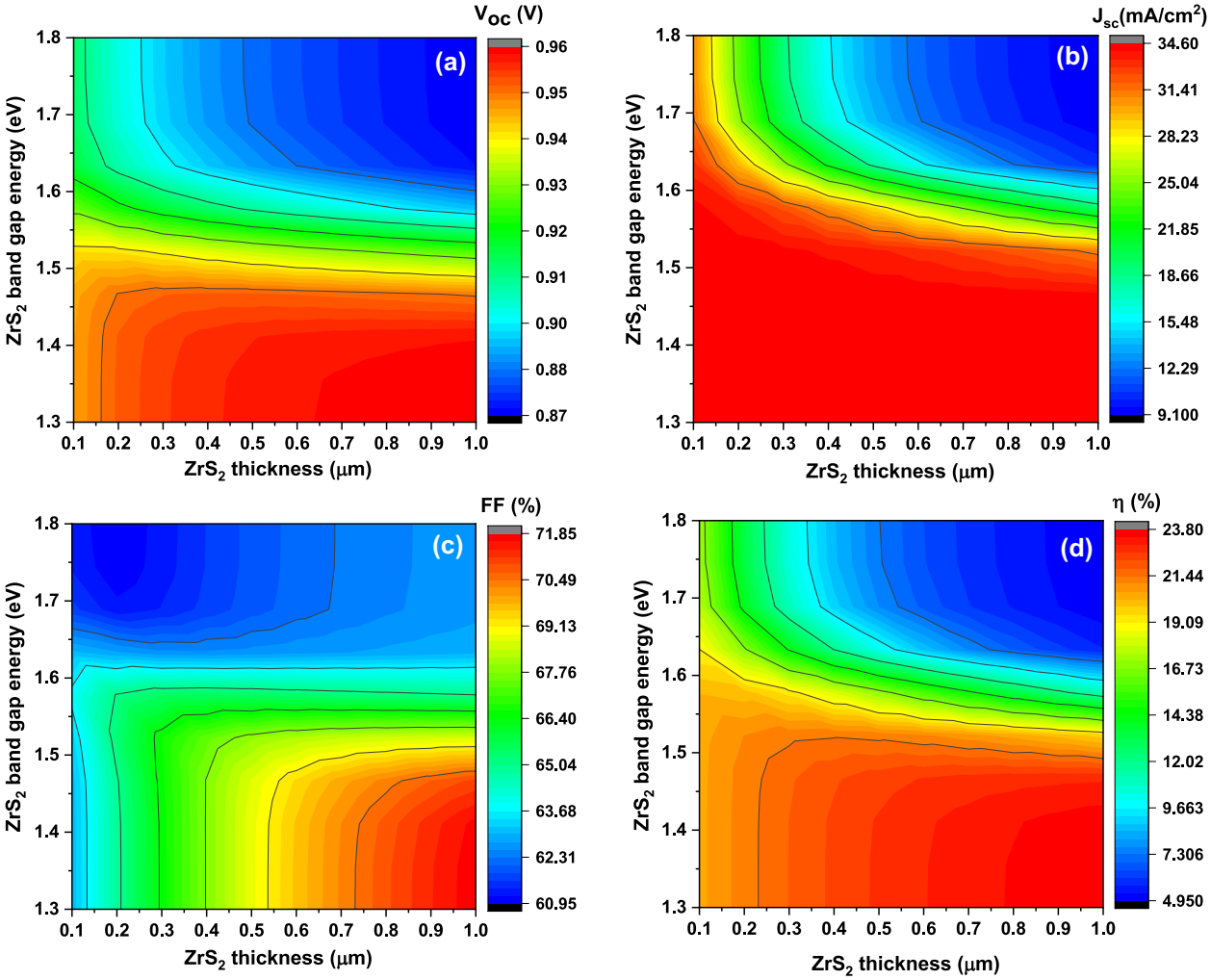


**Figure 6.** The simulated solar cells basic parameters including $V_{oc}$ (**a**), $J_{sc}$ (**b**), FF (**c**), and η (**d**) as function on the window layer thickness (x-axis) and the band gap (y-axis) at donor concentration $10^{19}$ $cm^{-3}$.

The obtained results could be elucidated as the band gap rising, more light path through interface junction and therefore increasing photogenerated rate for the charge carries and then separated and collected easily. At the same time the recombination current as well as the leakage current will be reduced. These factors will enhance the the $\mathbf{V_{oc}}$ value for band gap less than 1.45 eV as previously discussed as in Eq. (3)[37]. On the other hand the $\mathbf{V_{oc}}$ value increase with thickness increasing and therefore improvement of the charge collection length and consequently increasing of electron hole pairs generation through the junction[43]. Moreover, the alignment of bandgaps plays important role to improve the $\mathbf{V_{oc}}$ value where with small band gap for $ZrS_2$ than 1.45 eV more confinement take place and therefore the intra-band tunneling for carriers at the interface voltage barrier increases and more current generated[46]. The same description could be applied to explain the behavior of the $\mathbf{J_{sc}}$ values especially for band gap less than 1.55 eV.

By increasing the $ZrS_2$ band gap both the $\mathbf{V_{oc}}$ and the $\mathbf{J_{sc}}$ values reduce and this could be attributed to increasing of recombination process as well as the leakage current especially with increasing of $ZrS_2$ thickness[2,38]. In such case the mismatch between CuO band gap and $ZrS_2$ band gap produce capture centers which increasing the carrier recombination[38]. The behavior of the **FF** could be explained where it is a function on the $\mathbf{V_{oc}}$ values as shown in Eq. (4). The η values mainly followed the sum of the $\mathbf{V_{oc}}$, the $\mathbf{J_{sc}}$, and the **FF** values as presented in Eq. (4)[40].

From over results we decided that to have higher efficacies devices, the $ZrS_2$ thickness and band gap would be in the range from 0.7 to 1 μm and 1.4 eV, respectively. So, JV curves with basic parameters of solar cell devices as function of $ZrS_2$ thickness from 0.7 to 1 μm at fixed band gap of 1.4 eV are recorded as shown in Fig. 7. In this case, the $\mathbf{V_{oc}}$ has value from 0.96 to 0.97 V, the $\mathbf{J_{sc}}$ has constant value of 34.5 mA/cm$^2$, the **FF** has value from 70.28 to 71.7% and the **η** has value from 23.2 to 23.72% with increasing thickness from 0.7 to 1 μm, respectively.

Figure 8 demonstrates the contour plot of the solar cell basic parameters as a function on the $ZrS_2$ thin film thickness and the carrier concentration differ from 0.1 to 1 μm (the x-axis) and from $1\times10^{14}$ to $1\times10^{21}$ cm$^{-3}$ (the y-axis), respectively.

It is evident from Fig. 8a that the $\mathbf{V_{oc}}$ has different sectors depending mainly on the thickness of $ZrS_2$. For carrier concentration less than $10^{20}$ cm$^{-3}$, the $\mathbf{V_{oc}}$ grows from about 0.944 V to about 0.955 V with thickness increasing from 0.1 till 0.5 μm where the $\mathbf{V_{oc}}$ value is almost the same for each thickness. While for higher thickness, the $\mathbf{V_{oc}}$ value remains nearly constant at about 0.957 V. For carrier concentration of $10^{20}$ and $10^{21}$ cm$^{-3}$, the $\mathbf{V_{oc}}$ continues almost constant. In general, the $\mathbf{V_{oc}}$ value varies for different carrier concentration and thickness of $ZrS_2$ with only small range of about 0.02 V.

The $\mathbf{J_{sc}}$ value stays constant at about 34.5 mA/cm$^2$ for all different carrier concentration and thickness of $ZrS_2$ as presented in Fig. 8b. Only for carrier concentration of $10^{20}$ and $10^{21}$ cm$^{-3}$ and with higher thickness than 0.5 μm, the $\mathbf{J_{sc}}$ decreasing from about 34.5 mA/cm$^2$ to 31.5 mA/cm$^2$.

Figure 8c implies that the FF increases in sectors from about 61.5 to about 72.5% with thickness increasing and its value remains constant for each thickness with varying of carrier concentration till $10^{20}$ cm$^{-3}$. While for carrier concentration above $10^{20}$ cm$^{-3}$, the FF increase from about 70% to about 76%.

Figure 8d realizes that the η has different values with different sectors where it increases mainly from about 20% to about 23.5% with thickness increasing from 0.1 to 1 μm especially for carrier concentration less $10^{20}$ cm$^{-3}$ and remains constant for each thickness even with different carrier concentration. There is a curved path in which the η has the highest value from about 23.5% to 23.8%. This path located between thickness of 1 μm and from carrier concentration of $10^{14}$ cm$^{-3}$ to carrier $10^{20}$ cm$^{-3}$, then for higher carrier concentration above$10^{20}$ cm$^{-3}$ and with $ZrS_2$ thickness in the range from 0.3 to 1 μm.

It is clear that the increasing of donor concentrations of $ZrS_2$ thin film has no influence on the $\mathbf{V_{oc}}$ value especially with lower than $10^{20}$ cm$^{-3}$ with each individual thickness. This may be due to full formation of the depletion width ($\mathbf{W_d}$) which affected on the generation rate of charge carriers and the diffusion length of minority carriers

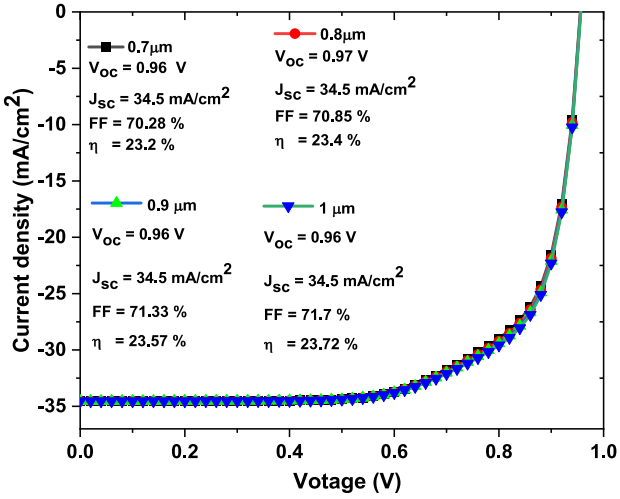


**Figure 7.** The simulated JV curves with basic parameters of solar cells as function on $ZrS_2$ thickness from 0.7 to 1 μm.

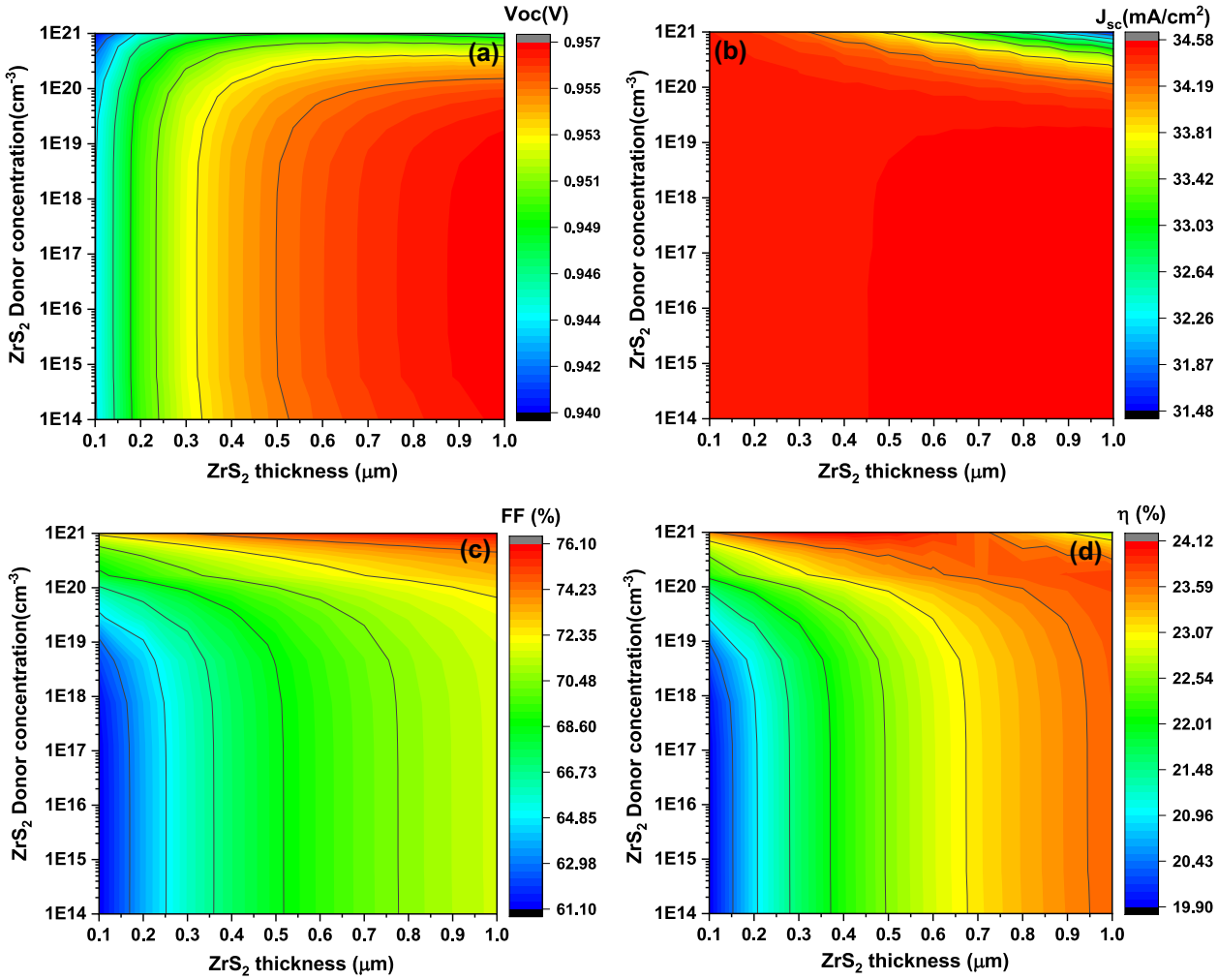


**Figure 8.** The simulated solar cells basic parameters including $V_{oc}$ (**a**), $J_{sc}$ (**b**), FF (**c**), and η (**d**) as function on the window layer thickness (x-axis) and the carrier concentration (y-axis).

(holes) in n-$ZrS_2$ and (electrons) in p-CuO[2]. So, the photogenerated current is completely related to depletion $\mathbf{W_d}$ and therefore full built-in voltage ($\mathbf{V_{bi}}$) which mainly constructed on the side of the p-CuO thin film[37]. On the other hand, the $\mathbf{V_{oc}}$ value increase with increasing of $ZrS_2$ thickness for each individual carrier concentration that could be attributed to increase the life time and length of charge collection leading more photogenerated current, therefore leakage current and recombination rate will decline with growing of thin film thickness[45].

Such suggestions are validated since the increasing of carrier concentration above $10^{20}$ cm$^{-3}$ produce almost constant value of the $\mathbf{V_{oc}}$ even with thickness increasing. Moreover, the constant value of the $\mathbf{J_{sc}}$ with increasing of both thickness and carrier concentration of $ZrS_2$ thin films supported such explanations. Also, the constant $\mathbf{J_{sc}}$ value due to that the window layer does not perform a huge part in the solar spectrum absorbing where it is mainly managed as conducting path for electrons[47].

The η values reflect the total behavior of the $\mathbf{V_{oc}}$, the $\mathbf{J_{sc}}$, and **FF** where its value mainly follows the $\mathbf{V_{oc}}$, and **FF**. The photogenerated current is investigated where EQE is simulated as function on $ZrS_2$ thickness, band gap, and the carrier concentration as stated in Fig. 9. It is certain that EQE value reduce from about 72% to around zero with increasing thickness from 0.1 to 1 μm at higher energy and from 100% to around 80% at lower energy. With raising of the band gap, the EQE value downward from 100 to 38% especially for higher wavelength. This reducing for EQE with increasing of thickness and band gap could be attributed to improving of the recombination rate and decreasing the charge carrier collection and therefore decline of the separation of the generated current[46]. The EQE has the same value and shape with different carrier concentration. EQE results are agreed and supported the obtained values of $\mathbf{J_{sc}}$ for $ZrS_2$ thin thilm thickness, band gap, and carrier concentrations.

Figure 10 describes the obtained JV curves with solar cell basic parameters with variation of $ZrS_2$ thin film thickness and carrier concentration. From Fig. 10a, the **η** value increase from 23.53 to 23.8% with thickness increasing from 0.7 to 1 μm, while the carrier concentration for $ZrS_2$ thin film is fixed at above$10^{20}$ cm$^{-3}$. On the other hand, from Fig. 10a and at constant $ZrS_2$ thickness of 1 μm So, the **η** value increase from 23.67 to 23.8% with increasing of carrier concentration from $10^{14}$ to $10^{20}$ cm$^{-3}$. Additionally, our simulations results indicate that to have higher efficiencies of inorganic $ZrS_2$/CuO heterojunction solar cell devices, the CuO band gap, thickness, and carrier concentration would be about 1.35 eV, 5.5 μm, and above $10^{18}$ cm$^{-3}$. While, the $ZrS_2$ band

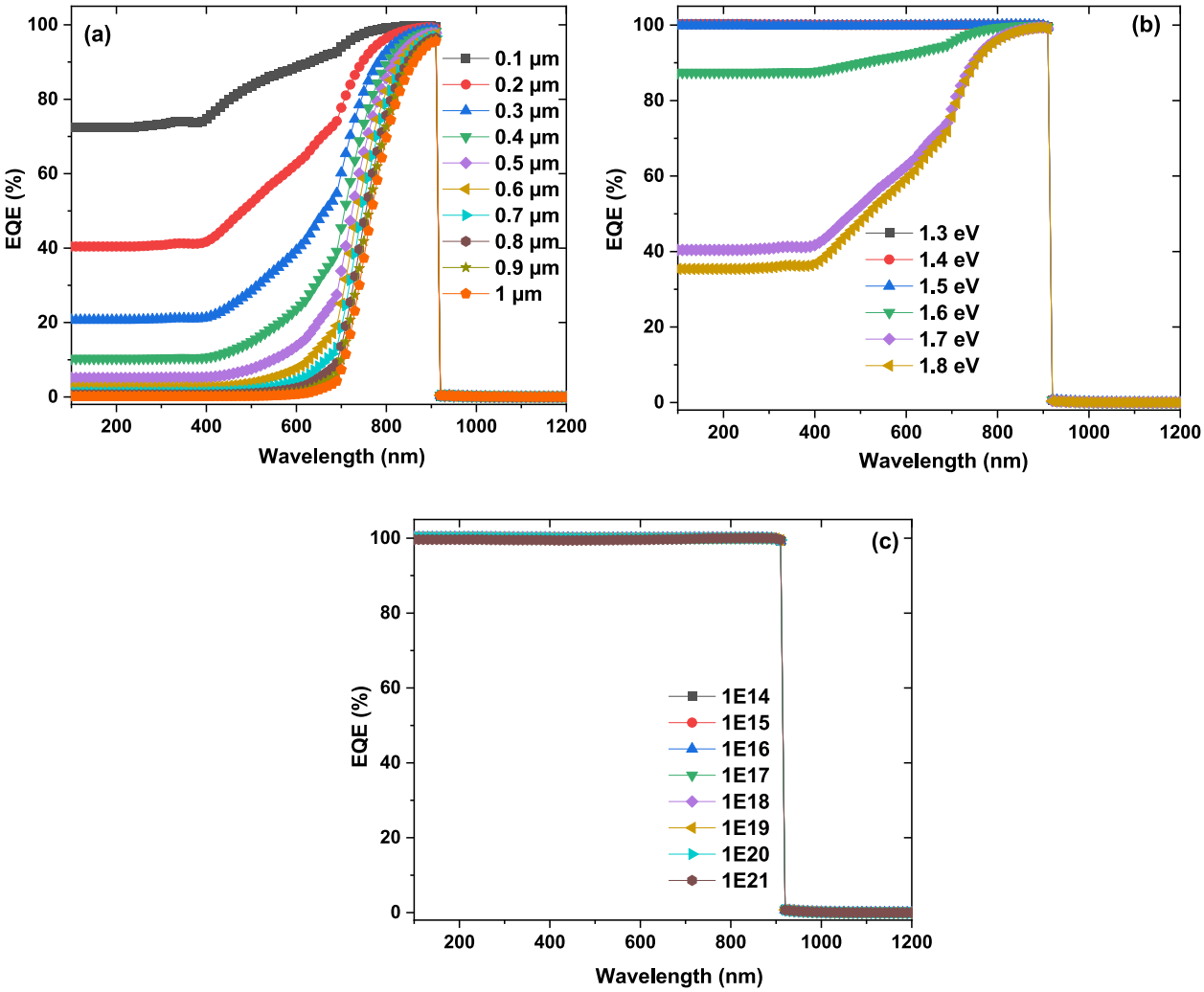


**Figure 9.** The simulated external quantum efficiency as function on $ZrS_2$ thickness (**a**), band gap (**b**), and the carrier concentration (**c**), respectively.

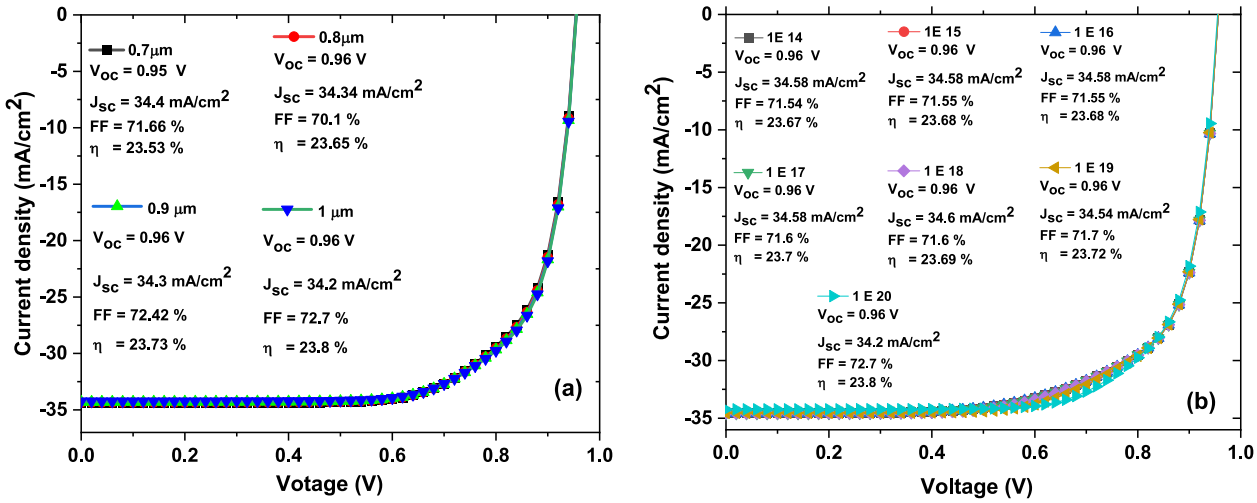


**Figure 10.** The simulated JV curves with basic parameters of solar cells as function on $ZrS_2$ thickness (**a**) and carrier concentration (**b**).

gap, thickness, and carrier concentration would be about 1.4 eV, 1 μm, and less than $10^{20}$ $cm^{-3}$ where the highest efficiency of about 23.8% was achieved with the $\mathbf{V_{oc}}$ value of 0.96 V, the $\mathbf{J_{sc}}$ value of 34.2 $mA/cm^2$, and the **FF** value of 72.2%. Our results indicate that $ZrS_2$/CuO solar cell devices could be comparable with one based on $In_2S_3$. The optimum devices of Cu(In, Ga)$Se_2$, CuIn(S,Se)$_2$ and $Cu_2ZnSnS_4$ based solar cells, where $In_2S_3$ was the buffer layer (50–125 nm thickness), fluorine-doped tin oxide was window layer and gold (Au) was used for back contact, revealed highest efficiencies in the range of 16.94–22.50%[49]. Additionally, Reyes et al. developed FTO/$TiO_2$/$MASnI_3$/$Cu_2ZnSnS_4$/Au as a *n-i-p* heterojunction perovskite solar cell[48]. They reported that when the acceptor and defect densities were $10^{16}$ $cm^{-3}$ and $10^{14}$ $cm^{-3}$, respectively, the best values ($\mathbf{V_{oc}}$ of 0.96 V, $\mathbf{J_{sc}}$ of 31.66 $mA/cm^2$, FF of 67% and **η** of 20.28%), were obtained[50].

**Impact of operation temperature on JV curves and the basic parameters of optimum $ZrS_2$/CuO solar cell.** In this section, the influence of operation temperature on JV curves and the basic parameters of the optimum $ZrS_2$/CuO solar cell was investigated as presented in Fig. 11. It is apparent that increasing of operation temperature minimize the $\mathbf{V_{oc}}$ and the $\mathbf{J_{sc}}$ and therefore the η where their values decreasing from 1.05 to 0.87 V, 34.5 to 33.6 $mA/cm^2$, and 24.8 to 22.1%, respectively with rising temperature from 260 to 340 K.

Such results could be explained employing Eq. (3) where the reverse saturation current ($\mathbf{I_o}$) increases by temperature increasing as well as the growing of the recombination probability for the charge carriers, and therefore the $\mathbf{V_{oc}}$, the $\mathbf{J_{sc}}$, and the η values reduce[44]. The results indicate small variation in the η value especially with the average temperature all over the world and consequently the applicable of $ZrS_2$/CuO solar cell to fabricate higher performance photovoltaic devices.

The explanations for the effect of carrier concentration and bandgap on the fundamental parameters of inorganic $ZrS_2$/CuO heterojunction solar cells could be cleared by the energy band diagram for the window and absorber layers as presented in Fig. 12[51,52]. The figure indicates that the valence band (VB) and conduction band (CB) energies of $ZrS_2$ and CuO thin films are with good match together which increasing of the generation and separation rates of generated the electron-hole pairs. In such case, when the heterojunction absorbing photons,

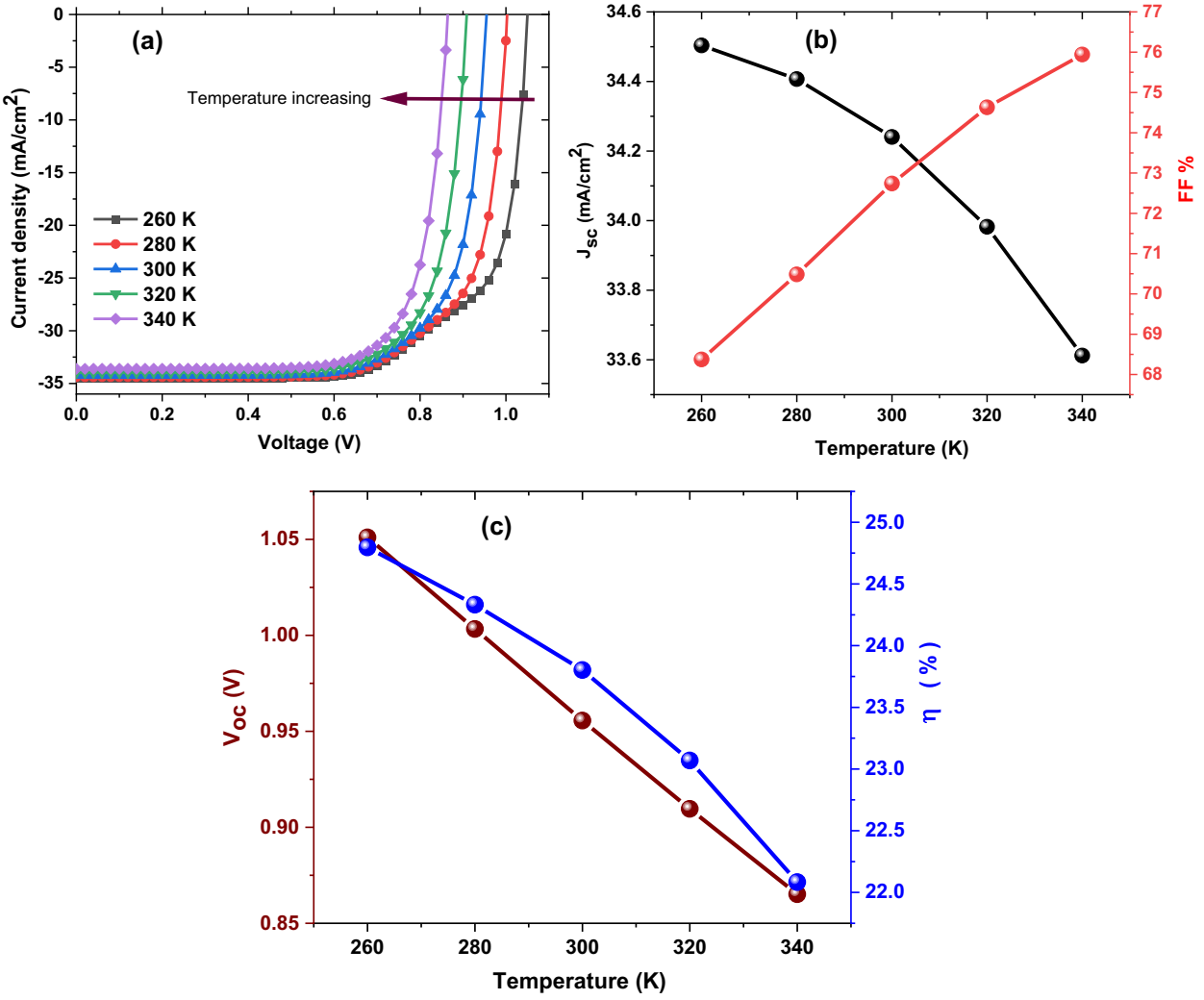


**Figure 11.** The simulated JV curves and the basic parameters of optimum $ZrS_2$/CuO solar cell as function on operation temperature (K).

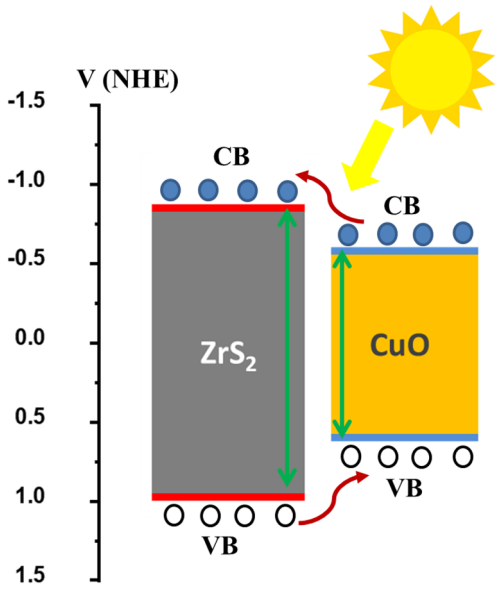


**Figure 12.** The schematic for the energy band diagram of inorganic $ZrS_2$/CuO heterojunction.

the electron-hole pairs generate and therefore electrons move from CB of CuO thin film to CB of $ZrS_2$ thin film while holes move from VB of $ZrS_2$ thin film to VB of CuO thin film then they are separated at the front and back contacts. By increasing the carrier concentration, the generation of electron-hole pairs will increase as well as the photocurrent. Moreover, when the band gaps values are 1.35 and 1.4 eV for $ZrS_2$ and CuO thin films, the alignment of band energies will increase and therefore the efficiency will greatly be enhanced.

## Conclusions

In conclusion, novel inorganic $ZrS_2$/CuO heterojunction solar cells was simulated for the first time using SCAPS-1D software. After successfully simulation process, the optimum thickness, carrier concentration, and bandgap for CuO thin film were found to be 1.35 eV, 5.5 µm, and above $10^{18}$ $cm^{-3}$, respectively, and for $ZrS_2$ thin film to be 1.4 eV, 1 µm, and less than $10^{20}$ $cm^{-3}$, respectively to have higher solar cell efficiency. Employing such parameters, the highest **η** of 23.8% was realized with the $\mathbf{V_{oc}}$ value of 0.96 V, the $\mathbf{J_{sc}}$ value of 34.2 mA/$cm^2$, and the **FF** value of 72.2%. The photogenerated current, the recombination rate, the collection charge carrier length, the minority carrier lifetime, width of the depletion layer, the built-in potential are the elements that manipulated the performance of solar cell basic parameters. Application of our simulation outcomes on the experimental area could help to obtain high-efficiency photovoltaic devices based on $ZrS_2$/CuO heterojunctions.

## Data availability

The datasets used and/or analysed during the current study available from the corresponding author on reasonable request.

Received: 5 January 2023; Accepted: 14 March 2023
Published online: 20 March 2023

## References

1. Jafarzadeh, F., Aghili, H., Nikbakht, H. & Javadpour, S. Design and optimization of highly efficient perovskite/homojunction SnS tandem solar cells using SCAPS-1D. *Sol. Energy* **236**, 195–205 (2022).
2. Moustafa, M., Al Zoubi, T. & Yasin, S. Exploration of CZTS-based solar using the ZrS2 as a novel buffer layer by SCAPS simulation. *Opt. Mater.* **124**, 112001 (2022).
3. Li, L. *et al.* High-performance Schottky solar cells using ZrS 2 nanobelt networks. *Energy Environ. Sci.* **4**, 2586–2590 (2011).
4. Chen, B. *et al.* Transition metal dichalcogenides for alkali metal ion batteries: Engineering strategies at the atomic level. *Energy Environ. Sci.* **13**, 1096–1131 (2020).
5. Patel, M., Pataniya, P. M., Patel, V., Sumesh, C. K. & Late, D. J. Large area, broadband and highly sensitive photodetector based on ZnO-WS2/Si heterojunction. *Sol. Energy* **206**, 974–982. https://doi.org/10.1016/j.solener.2020.06.067 (2020).
6. Gautam, C., Verma, A., Chaudhary, P. & Yadav, B. C. Development of 2D based ZnO–MoS2 nanocomposite for photodetector with light-induced current study. *Opt. Mater.* **123**, 111860. https://doi.org/10.1016/j.optmat.2021.111860 (2022).
7. Anju, S. & Mohanan, P. V. Biomedical applications of transition metal dichalcogenides (TMDCs). *Synthetic Metals* **271**, 116610. https://doi.org/10.1016/j.synthmet.2020.116610 (2021).
8. Guo, H. *et al.* Two-dimensional WO3-transition-metal dichalcogenide vertical heterostructures for nitrogen fixation: A photo (electro) catalysis theoretical strategy. *J. Phys. Chem. C* **126**, 3043–3053. https://doi.org/10.1021/acs.jpcc.1c09772 (2022).
9. Li, Y. *et al.* Intercalation assisted liquid phase production of disulfide zirconium nanosheets for efficient electrocatalytic dinitrogen reduction to ammonia. *Green Energy Environ.* https://doi.org/10.1016/j.gee.2022.01.009 (2022).
10. Vu, T. V. *et al.* Electronic properties and optical behaviors of bulk and monolayer ZrS2: A theoretical investigation. *Superlattices Microstruct.* **125**, 205–213. https://doi.org/10.1016/j.spmi.2018.11.008 (2019).

11. Hamada, M. *et al.* ZrS2 symmetrical-ambipolar FETs with near-midgap TiN film for both top-gate electrode and Schottky-barrier contact. *Jpn. J. Appl. Phys.* **60**, SBBH05 (2021).
12. Kim, S., Kim, Y. J. & Ryu, W.-H. Zirconium disulfides as an electrode material alternative for Li-ion batteries. *Appl. Surf. Sci.* **547**, 149029. https://doi.org/10.1016/j.apsusc.2021.149029 (2021).
13. Mattinen, M. *et al.* Atomic layer deposition of emerging 2D semiconductors, HfS2 and ZrS2, for optoelectronics. *Chem. Mater.* **31**, 5713–5724. https://doi.org/10.1021/acs.chemmater.9b01688 (2019).
14. Wen, Y., Zhu, Y. & Zhang, S. Low temperature synthesis of ZrS 2 nanoflakes and their catalytic activity. *RSC Adv.* **5**, 66082–66085 (2015).
15. Tang, W. *et al.* Antifriction and antiwear effect of lamellar ZrS2 nanobelts as lubricant additives. *Nanomaterials* **9**, 329. https://doi.org/10.3390/nano9030329 (2019).
16. Tian, Y. *et al.* Epitaxial growth of large area ZrS2 2D semiconductor films on sapphire for optoelectronics. *Nano Res.* https://doi.org/10.1007/s12274-022-4308-4 (2022).
17. Shimazu, Y., Fujisawa, Y., Arai, K., Iwabuchi, T. & Suzuki, K. Synthesis and characterization of zirconium disulfide single crystals and thin-film transistors based on multilayer zirconium disulfide flakes. *ChemNanoMat* **4**, 1078–1082 (2018).
18. Mattinen, M. *et al.* Van der Waals epitaxy of continuous thin films of 2D materials using atomic layer deposition in low temperature and low vacuum conditions. *2D Mater.* **7**, 011003 (2019).
19. Hamada, M. *et al.* High hall-effect mobility of large-area atomic-layered polycrystalline ZrS 2 film using UHV RF magnetron sputtering and sulfurization. *IEEE J. Electron Devices Soc.* **7**, 1258–1263 (2019).
20. El-Sayed, S. & Sayed, A. M. E. Preparation and characterization of CuO/Co3O4/poly(methyl methacrylate) nanocomposites for optical and dielectric applications. *J. Mater. Sci.* **32**, 13719–13737. https://doi.org/10.1007/s10854-021-05949-9 (2021).
21. Shaban, M., Abdelkarem, K. & El Sayed, A. M. Structural, optical and gas sensing properties of Cu2O/CuO mixed phase: Effect of the number of coated layers and (Cr + S) co-Doping. *Phase Transit.* **92**, 347–359. https://doi.org/10.1080/01411594.2019.1581886 (2019).
22. El-Shafai, N. M., Ibrahim, M. M., Abdelfatah, M., Ramadan, M. S. & El-Mehasseb, I. M. Synthesis, characterization, and cytotoxicity of self-assembly of hybrid nanocomposite modified membrane of carboxymethyl cellulose/graphene oxide for photocatalytic antifouling, energy storage, and supercapacitors application. *Colloids Surf. A* **626**, 127035. https://doi.org/10.1016/j.colsurfa.2021.127035 (2021).
23. Abdelfatah, M. *et al.* Insight into Co concentrations effect on the structural, optical, and photoelectrochemical properties of ZnO rod arrays for optoelectronic applications. *J. Alloys Compd.* **873**, 159875. https://doi.org/10.1016/j.jallcom.2021.159875 (2021).
24. Ismail, W., El-Shafai, N. M., El-Shaer, A. & Abdelfatah, M. Impact of substrate type on the surface and properties of electrodeposited Cu2O nanostructure films as an absorber layer for solar cell applications. *Mater. Sci. Semicond. Process.* **120**, 105335. https://doi.org/10.1016/j.mssp.2020.105335 (2020).
25. Abdelfatah, M., El-Shafai, N. M., Ismail, W., El-Mehasseb, I. M. & El-Shaer, A. in*IOP Conference Series: Materials Science and Engineering.* 012005 (IOP Publishing).
26. Pindolia, G., Shinde, S. M. & Jha, P. K. Optimization of an inorganic lead free RbGeI3 based perovskite solar cell by SCAPS-1D simulation. *Sol. Energy* **236**, 802–821. https://doi.org/10.1016/j.solener.2022.03.053 (2022).
27. Jiao, Y. *et al.* Towards high sensitivity infrared detector using Cu2CdxZn1-xSnSe4 thin film by SCAPS simulation. *Sol. Energy* **225**, 375–381. https://doi.org/10.1016/j.solener.2021.07.044 (2021).
28. Karthick, S., Velumani, S. & Bouclé, J. Experimental and SCAPS simulated formamidinium perovskite solar cells: A comparison of device performance. *Sol. Energy* **205**, 349–357. https://doi.org/10.1016/j.solener.2020.05.041 (2020).
29. Fatema, K. & Arefin, M. S. Enhancing the efficiency of Pb-based and Sn-based perovskite solar cell by applying different ETL and HTL using SCAPS-1D. *Opt. Mater.* **125**, 112036. https://doi.org/10.1016/j.optmat.2022.112036 (2022).
30. Ouédraogo, S., Zougmoré, F. & Ndjaka, J. Numerical analysis of copper-indium-gallium-diselenide-based solar cells by SCAPS-1D. *Int. J. Photoenergy* **2013**, 1–9 (2013).
31. Wanda, M. D., Ouédraogo, S., Tchoffo, F., Zougmoré, F. & Ndjaka, J. Numerical investigations and analysis of Cu2ZnSnS4 based solar cells by SCAPS-1D. *Int. J. Photoenergy* **2016**, 1–9 (2016).
32. Burgelman, M., Nollet, P. & Degrave, S. Modelling polycrystalline semiconductor solar cells. *Thin Solid Films* **361**, 527–532 (2000).
33. Burgelman, M., Verschraegen, J., Degrave, S. & Nollet, P. Modeling thin-film PV devices. *Prog. Photovolt.* **12**, 143–153 (2004).
34. Mostefaoui, M., Mazari, H., Khelifi, S., Bouraiou, A. & Dabou, R. Simulation of high efficiency CIGS solar cells with SCAPS-1D software. *Energy Procedia* **74**, 736–744 (2015).
35. Abdelfatah, M., Ismail, W., El-Shafai, N. M. & El-Shaer, A. Effect of thickness, bandgap, and carrier concentration on the basic parameters of Cu2O nanostructures photovoltaics: Numerical simulation study. *Mater. Technol.* **36**, 712–720 (2021).
36. El-Shafai, N. M. *et al.* Enhancement of electrochemical properties and photocurrent of copper oxide by heterojunction process as a novel hybrid nanocomposite for photocatalytic anti-fouling and solar cell applications. *Sep. Purif. Technol.* **267**, 118631 (2021).
37. Abdelfatah, M. *et al.* Fabrication and characterization of low cost Cu 2 O/ZnO: Al solar cells for sustainable photovoltaics with earth abundant materials. *Sol. Energy Mater. Sol. Cells* **145**, 454–461 (2016).
38. Lin, W. M. *et al.* Simulating nanocrystal-based solar cells: A lead sulfide case study. *J. Chem. Phys.* **151**, 241104 (2019).
39. Mbopda Tcheum, G. L., Teyou Ngoupo, A., OuÉDraogo, S., Guirdjebaye, N. & Ndjaka, J. M. B. Numerical analysis of ultrathin Cu(In, Ga)Se$$_{2}$$solar cells with Zn(O, S) buffer layer. *Pramana* **94**, 111. https://doi.org/10.1007/s12043-020-01977-y (2020).
40. Baloch, A. A. *et al.* Full space device optimization for solar cells. *Sci. Rep.* **7**, 11984 (2017).
41. Brus, V. V., Solovan, M. M., Schopp, N., Kaikanov, M. & Mostovyi, A. I. Visible to near-infrared photodiodes with advanced radiation resistance. *Adv. Theory Simul.* **5**, 2100436 (2022).
42. Schopp, N., Brus, V. V., Lee, J., Bazan, G. C. & Nguyen, T. Q. A Simple approach for unraveling optoelectronic processes in organic solar cells under short-circuit conditions. *Adv. Energy Mater.* **11**, 2002760 (2021).
43. Al-Hattab, M., Khenfouch, M., Bajjou, O., Chrafih, Y. & Rahmani, K. Numerical simulation of a new heterostructure CIGS/GaSe solar cell system using SCAPS-1D software. *Sol. Energy* **227**, 13–22 (2021).
44. Chen, A. & Zhu, K. Computer simulation of a-Si/c-Si heterojunction solar cell with high conversion efficiency. *Sol. Energy* **86**, 393–397 (2012).
45. Musselman, K. P., Marin, A., Schmidt-Mende, L. & MacManus-Driscoll, J. L. Incompatible length scales in nanostructured $Cu_2O$ solar cells. *Adv. Func. Mater.* **22**, 2202–2208 (2012).
46. Verschraegen, J. & Burgelman, M. Numerical modeling of intra-band tunneling for heterojunction solar cells in SCAPS. *Thin Solid Films* **515**, 6276–6279 (2007).
47. Zhu, L., Shao, G. & Luo, J. Numerical study of metal oxide hetero-junction solar cells with defects and interface states. *Semicond. Sci. Technol.* **28**, 055004 (2013).
48. Gupta, G. K. & Dixit, A. Theoretical studies of single and tandem $Cu_2ZnSn\ (S/Se)_4$ junction solar cells for enhanced efficiency. *Opt. Mater.* **82**, 11–20 (2018).
49. Ashraf, M. A. & Alam, I. Numerical simulation of CIGS, CISSe and CZTS-based solar cells with $In_2S_3$ as buffer layer and Au as back contact using SCAPS 1D. *Eng. Res. Express* **2**, 035015. https://doi.org/10.1088/2631-8695/abade6 (2020).
50. Piñón Reyes, A. C. *et al.* Study of a lead-free perovskite solar cell using CZTS as HTL to achieve a 20% PCE by SCAPS-1D simulation. *Micromachines* **12**, 1508 (2021).

51. Jung, K. *et al.* ZnO-CuO core-shell heterostructure for improving the efficiency of ZnO-based dye-sensitized solar cells. *MRS Adv.* **15**, 857–862 (2017).
52. Krishnakumar, B., Imae, T., Miras, J. & Esquena, J. Synthesis and azo dye photodegradation activity of ZrS2–ZnO nano-composites. *Sep. Purif. Technol.* **132**, 281–288 (2014).

## Acknowledgements
The authors would like to thank Prof. Dr. Marc Burgelman, University of Gent, Belgium, for providing the SCAPS simulation software. Funded and supported by Science, Technology & Innovation Funding Authority (STDF) (Project ID: 37212) is gratefully acknowledged.

## Author contributions
All authors wrote the main manuscript text and reviewed the manuscript.

## Funding
Open access funding provided by The Science, Technology & Innovation Funding Authority (STDF) in cooperation with The Egyptian Knowledge Bank (EKB).

## Competing interests
The authors declare no competing interests.

## Additional information
**Correspondence** and requests for materials should be addressed to M.A. or A.E.-S.

**Reprints and permissions information** is available at www.nature.com/reprints.

**Publisher's note** Springer Nature remains neutral with regard to jurisdictional claims in published maps and institutional affiliations.